Graduate University of Advanced Technology

Journal of Geological Remote Sensing

Journal homepage: https:// jgrs.kgut.ac.ir

Iranian Geological Remote Sensing Society

Potential Assessment of Metal Minerals Using Statistical Processing and Hierarchical Analysis in the Ferdows-Gonabad-Bajestan region

Zohreh Arjomand Lary[1], Mehdi Honarmand*[2], Mahdieh Hosseinjanizadeh[3], Hadi Shahriari[4]

[1,2,3]Department of Ecology, Institute of Science and High Technology and Environmental Sciences Graduate University of Advanced Technology, Kerman, Iran.

[4]Department of Mining Engineering, Vali-e-Asr University of Rafsanjan, Rafsanjan, Iran

Article Info

Keywords:
Statistical processing,
Fault,
Photolineament factor,
AHP method,
Ferdows-Gonabad-Bajestan region

Abstract

This research aimed to evaluate the potential of ore mineralization in the Ferdows-Gonabad-Bajestan metallogenic zone, Khorasan Razavi province. Identification of hydrothermal alterations and structural zones was performed using satellite data. The ASTER and OLI satellite images were utilized to enhance hydrothermal alteration zones employing band ratio and principal component analysis (PCA) methods. The Sentinel-2A images were used to identify geological units and faults. The photolineament factor was produced to present the density of faults and fractures in the study area. Stream sediment and rock samples were examined for Ag, As, Au, Co, Cu, Fe, Mo, Pb, V, and Zn elements. The geology, geological structure, hydrothermal alteration, and geochemistry layers were combined using fuzzy OR operators. Subsequently, all data were valued using the analytical hierarchy process, weighed, and integrated with GIS software. Based on the results, five areas were identified as mineral potential zones, among which areas A, B, and C have a higher probability of ore mineralization. Field observation, thin section study, and XRD analysis were conducted to validate the results.

*Corresponding author: Mehdi Honarmand

Email: m.honarmand@kgut.ac.ir

https://doi.org/10.48306/jgrs.2025.464902.1008

Received April 2025; Accepted September 2025

1. Introduction

Remote sensing data can be utilized to specify mineralization zones using multi-spectral and multi-temporal coverage (Shahriari et al., 2015; Gupta., 2003). Indeed, remote sensing plays a crucial role in the early stages of mineral exploration campaigns, particularly in prospecting and mineral potential assessment in arid and semi-arid areas (Ghorbani et al., 2019; Ranjbar & Shahriari., 2006; Mousavi et al., 2019). Remote sensing sensors generate images in various electromagnetic spectrum ranges relying on the spectral signature of the target (Honarmand et al., 2011). Geological structures, geological units, and hydrothermal alterations can be derived from these images. Moreover, they can be highly cost-effective and time-saving in updating geological maps, improving map quality, and producing thematic maps such as hydrothermal alteration zones, geological units, lineaments, and fracture patterns (Tangestani et al., 2002). Establishing the quantitative and qualitative correlation between identified hydrothermal alteration zones and structural elements stands as a paramount factor of the mineral exploration programs (Mousavi et al., 2019). These operations hold significant importance, particularly in the mining areas abundant with structural and geological features.

The Ferdows-Gonabad-Bajestan region located in the southwest of Khorasan Razavi province presents fair evidences for mineral exploration based on previous and recent geological studies. There is no approved documents about the result of systematic mineral exploration activities in the area (Arjmand et al., 2023).

This study employes regional exploratory investigations including geology, remote sensing, and geochemistry studies. Advanced Spaceborne Thermal Emission and Reflection Radiometer (ASTER) and Operational Land Imager (OLI) images were utilized to identify hydrothermal alteration zones. band ratio and principal component analysis (PCA) are employed. Band ratio satisfies detecting alteration zones by using spectral bands related to index minerals of various alteration types like phyllic, argillic, and propylitic (Ahmadirouhani et al., 2018). In the PCA method, alteration mapping can be done by minimizing the effect of other phenomena (Honarmand et al., 2012; Carrino et al., 2015). PCA uses all bands or only specific bands of a sensor that signify a phenomenon (selective PCA). Selective PCA can be utilized for enhancing a specific type of hydrothermal alteration (Tözün et al., 2020; Mars & Rowan., 2006). This study performs the selective PCA method. Generally, faults and fractures control the extent and intensity of mineralization within a region. Therefore, to examine the status of faults and their relation with the supposed mineralization, the photolineament factor (PF) method is utilized. In addition, Sentinel-2A images are employed to detect faults in the area. Finally, a map depicting mineral potential is prepared using the analytical hierarchy process (AHP) method to prepare the geological, alteration, structural, and geochemical layers in the Ferdows-Gonabad-Bajestan region (Arjmand et al., 2023).

2. Study area

The study area is located in the highlands between the three cities; Ferdows, Gonabad, and Bajistan; situated in the south of Razavi Khorasan and the north of Lut block. This area is very different in lithology and includes igneous, sedimentary, and partially metamorphic rocks. The main lithology of the region comprises igneous rocks, mostly andesite, phyllite, and rhyolite. The sedimentary rocks are mainly limestone, dolomite, sandstone, conglomerate, and metamorphic rocks of quartzite type (Aganbati., 2006).

Geological data were extracted from 1:100,000 geological maps of Ferdows, Gonabad, Taherabad, Bajestan, Qasemabad, and Mahneh, prepared by the Geological Survey of Iran (GSI). Accordingly, the geology layer was established by digitizing faults and geological units.

The eastern central region of Iran is divided into two parts, a western part called the 'Lut Block' and a heavily folded eastern part known as the 'Eastern Iranian Mountain Range'. The Lut Block has a north-south trend extending from the Jazmurian wetland in the south to Gonabad in the north, spanning 800 km in length and 200-250 km in width. Its eastern border is marked by the Nehbandan Fault and its western border lies along the Nayband Fault (Fig. 1) (Aganbati., 2006). Mineralization in the Lut Block is attributed to the intrusion of Cenozoic magmatic rocks such as granite, diorite, and volcanic rocks. Vein-type mineralization of copper (Cu), lead (Pb), zinc (Zn), antimony (Sb), mercury (Hg), and gold (Au) have been reported in this area such as the Qaleh-Zari Cu-Au and Shurab-Kalleh Neginan Sb-Hg deposits (Ahmadirouhani., 2018). The study area is situated in Khorasan Razavi, between the cities of Ferdows, Gonabad, and Bajestan. Geologically, the area belongs to the northern part of the Lut Block. The primary lithological units consist of the igneous rocks and the sedimentary units (Fig. 1). Andesite and dacite are the main igneous rocks and widespread sedimentary rocks include carbonate rocks, dolomite, sandstone, and conglomerate. The trend of rock outcrops in this area extends from north-northwest to south-southwest which indicates the continuation of the central Iranian mountain range. Most of the rocks are of Tertiary age, exposed in various forms such as volcanic mountains and cones, hydrothermally altered zones, and volcanic breccia.

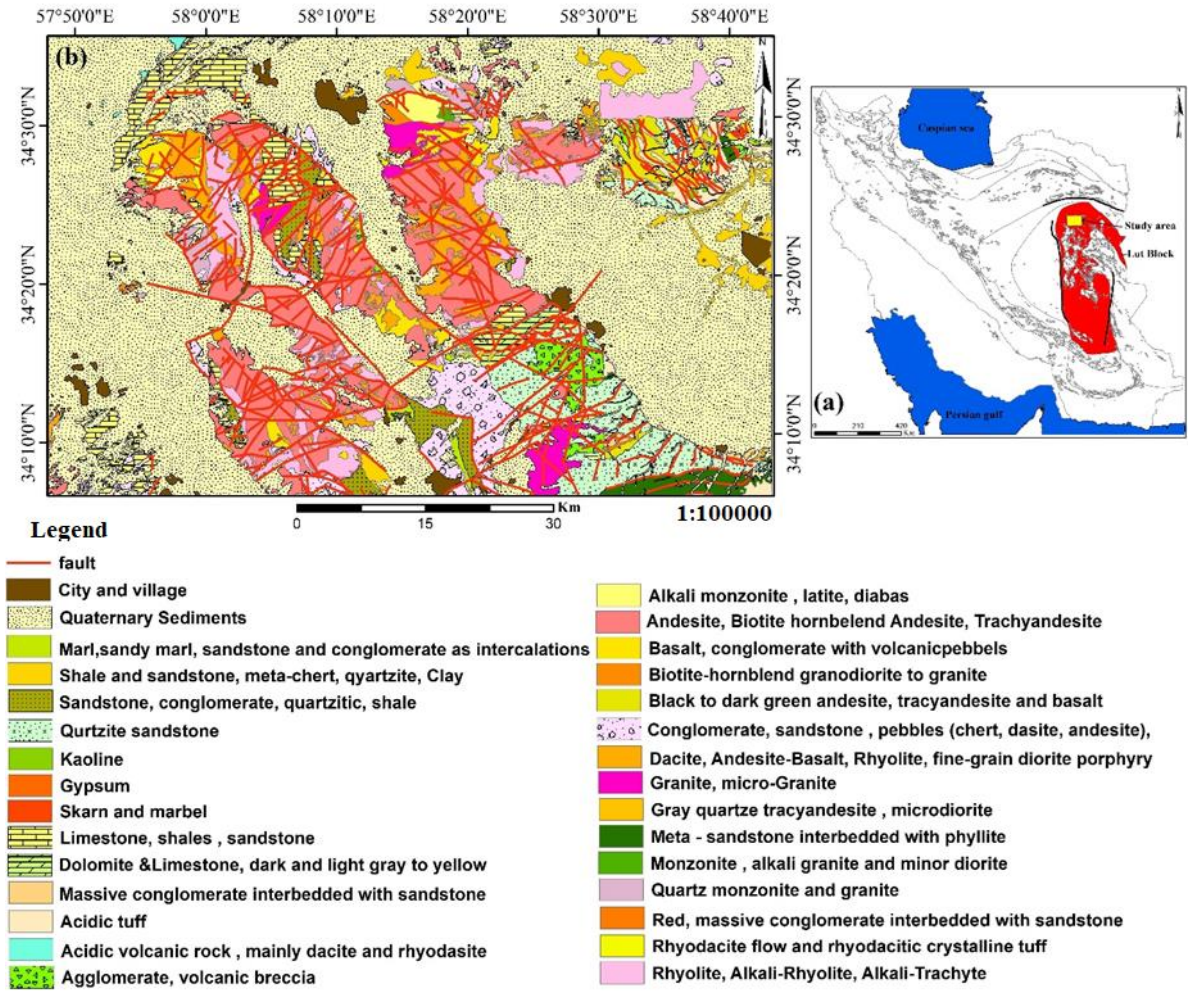

Figure 1- Geological map of the study area, 1:100000 (GSI, 2001)

3. Material and methods

3.1. Satellite data and image processing methods

OLI sensor data

The Landsat-8 satellite was launched into Earth's orbit on February 11, 2013. This satellite is the latest series of Landsat with two imaging sensors, OLI and TIRS. The OLI sensor has 9 bands where 8 of which have a spatial resolution of 30m with a panchromatic band of 15m (Roy et al 2014). The used OLI images were captured on July 13, 2019. OLI images have been utilized for identifying geological units and specifying oxidized and hydroxide minerals.

ASTER sensor data

The Terra satellite carries five sensors, among which one of the most significant is the Advanced Spaceborne Thermal Emission and Reflection Radiometer (ASTER). ASTER was launched into space in December 1999 and its imaging commenced in March 2000 (Abrams et al., 2015; Fujisada., 1995).

The ASTER sensor consists of 14 spectral bands: 3 bands with a spatial resolution of 15m in the visible and near-infrared (VNIR) range, 6 bands with a spatial resolution of 30m in the shortwave infrared (SWIR) range, and 5 bands with a resolution of 90m in the thermal infrared (TIR) range. The used VNIR+SWIR ASTER images were taken on July 10, 2019. The VNIR+SWIR bands of ASTER were applied for mapping hydrothermal alteration in the study area.

Sentinel-2A Satellite data

The Sentinel-2 mission comprises two imaging satellites including Sentinel-2A and Sentinel-2B. Sentinel-2A is presently in orbit and actively capturing images of the Earth (Abrams et al., 2015). These images have variable spatial resolution ranging from 10 m to 60 m and include 13 bands in the visible, near-infrared (NIR), and SWIR spectral ranges. The used Sentinel-2A images were captured on July 12, 2019. The Sentinel-2A images have been utilized for initial fault filtering and geological studies.

3.2. Satellite Image Processing

Color Composite

Constructing color composites is a simple and applicable method to enhance desired features using three bands of a sensor. True color composites (FCCs) use blue, green, and red bands of a sensor in the same colors to produce RGB images. False color composites (FCCs) apply visible bands in non-homonymous colors or non-visible channels of a sensor in RGB colors to enhance targeted features. Color composites offer a primary evaluation of the study area and serve as the foundation for other methods to enhance the targets (Drury., 1993).

Band Ratio Analysis

Band ratio involves dividing the brightness values of one spectral band by another. This method detects variations that cannot be demonstrated in a single band alone. Band ratio illustrates changes in the slope of spectral reflectance curves between two bands (Mars & Rowan., 2006). Hence, it is employed to differentiate lithological units and identify rocks. The recognition of reflective characteristics of targeted features is a base for using the band ratio method.

Principal Component Analysis (PCA)

Different bands of multispectral remote sensing images often exhibit correlations, meaning that most regions that appear bright or dark in one band present similar features in other bands. PCA extracts or minimizes redundant information by compressing multispectral datasets into a new coordinate system. This method is employed to reduce the interference effects of materials, especially vegetation cover, and extensively for mapping hydrothermal alterations in metallogenic zones (Honarmand et al., 2013). PCA can be conducted in two forms: standard principal component analysis (using all bands) and selective principal component analysis (Crosta method) which uses bands with absorption and reflection features of the desired target(s).

4- Results

4.1. RGB Color Combination

The conventional method used to identify different regions in remote sensing is the RGB color combination method. This process provides an initial overview of the hydrothermal alterations and lithological units in the study area. Since the ASTER sensor lacks a blue channel, which is crucial for detecting iron oxides, the OLI sensor has been utilized for this purpose. FCCs were used to detect the lithological units and vegetation cover (Table 2). Finally, the result was compared with the geological map of the area.

Table 2- False color combinations used in this study

Sensor	Used bands (RGB)	Description
ASTER	468	Propylitic alteration and limestone in yellow, phyllic, and argillic alterations in pink
OLI	753	Carbonate units in cyan, andesite units in dark brown, and kaolinite in yellow

Based on Table 2, FCC 468 has been applied to the ASTER image. Propylitic alteration is enhanced in yellow while phyllic and argillic alterations are detected in pink. Agricultural lands and vegetation cover in the area are depicted in brown (Figure 4a). Figure 4b displays FCC 753 from the OLI image where carbonate units are shown in cyan, andesitic units in dark brown, and the kaolinite unit in bright yellow. The reason for using FCCs is to provide a clearer depiction of lithological units and regional variations.

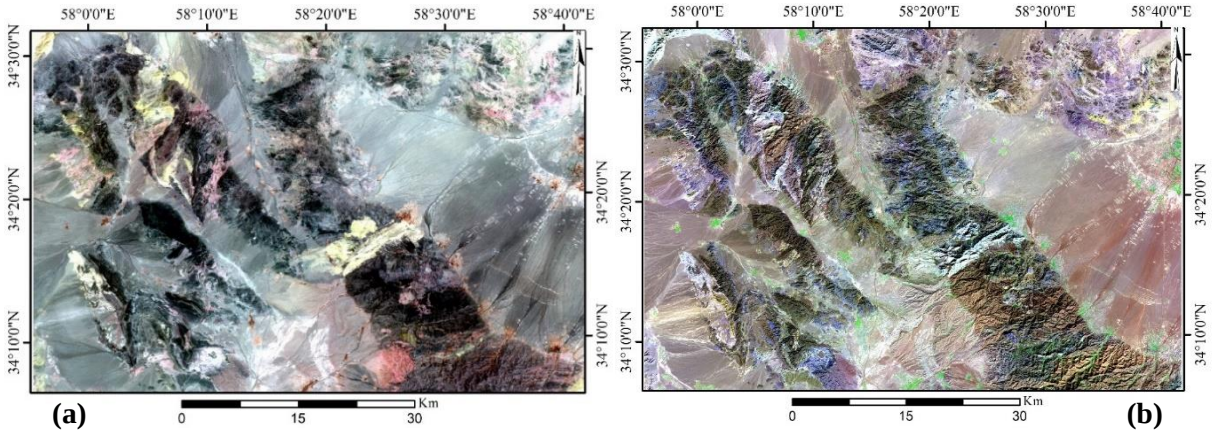

Figure 4- a) FCC 468 of the ASTER sensor. B) FCC 357 of the OLI sensor

4.2. Band Ratio (BR)

Band ratio is one of the widely used methods in image processing method which eliminates topographic effects and shadows. In this study, the spectral reflectance curves of minerals were used to identify absorption and reflective wavelengths to determine the appropriate band ratios for mineral mapping.

Table 3- Band ratios used in this study

Target	Sensor	Band ratio
Phyllic	ASTER	4+7/6
Argillic	ASTER	4+6/5
Propylitic	ASTER	7+9/8
Iron oxide and hydroxide minerals	OLI	4/2
Hydroxyl group minerals	OLI	6/7

Target areas were highlighted in bright pixels after applying band ratios. The density slicing technique was utilized for better visualization of targets.

Based on Table 3, the OLI band ratio of 2/4 was used to detect iron oxide minerals, and a band ratio of 6/7 was used to detect hydroxyl group minerals. Accordingly, oxide and hydroxyl group minerals (hydroxyl groups were detected alongside carbonates due to their limited bands in the SWIR) were detected with bright colors. The resulting colors for ease of interpretation and better visualization changed to yellow and red colors using the density slicing method. The result of the 4/2 band ratio compared with the geological map of the area indicates that iron oxide minerals are more prevalent in intrusive bodies such as granitoids and dacites and less in some sandstone and sedimentary units (Figure 5a). In the 7/6 band ratio image, areas with hydroxyl group minerals are mostly detected in granitic and rhyolitic rocks in the region (Figure 5b).

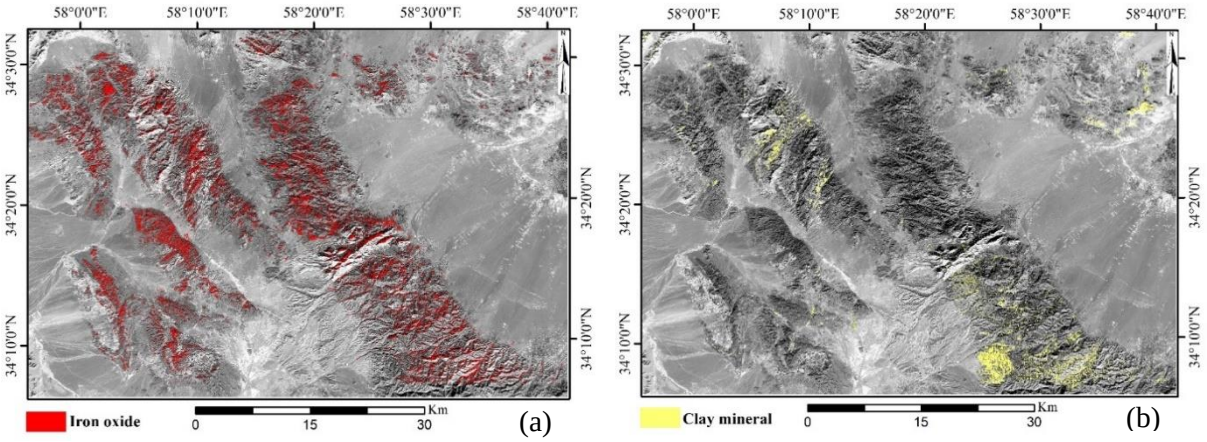

Figure 5- a) OLI 4/2 band ratio for detecting iron oxides. B) OLI 7/6 band ratio for detecting clay minerals in the study area.

The ASTER sensor was used to detect phyllic, argillic, and propylitic alterations. Phyllic alteration was detected with a band ratio of (6/7+4), argillic alteration with a band ratio of (5/6+4), and propylitic alteration with a band ratio of (8/9+7) (Table 2). The results indicate that phyllic alteration is more prevalent in granitoid rocks, argillic alteration mainly occurs in areas with rhyolitic and dacitic rocks, and propylitic alteration is observed in andesitic units (Figure 6).

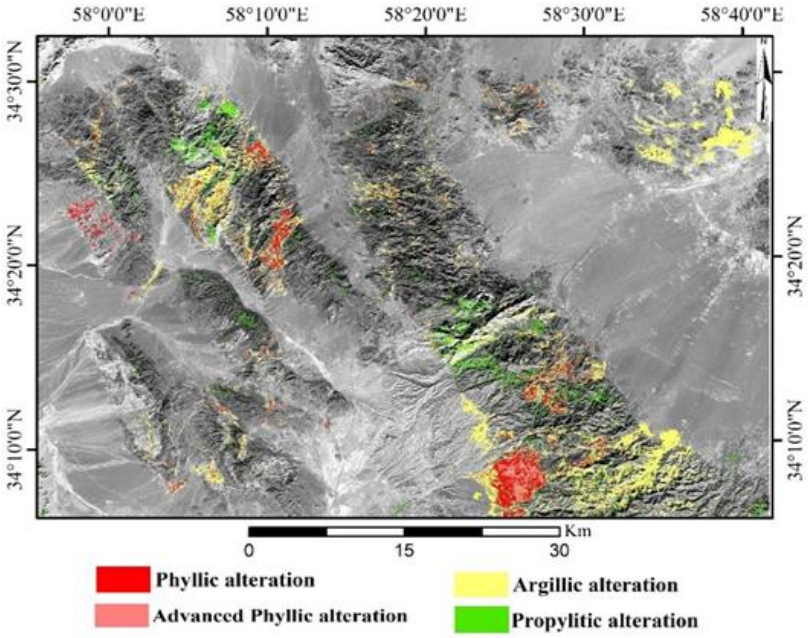

Figure 6- Different band ratios of ASTER for detecting phyllic, argillic, and propylitic alterations.

4.3. Principal Component Analysis (PCA) Using Crosta Method

Based on the index minerals spectra of the propylitic alteration, bands 6, 7, 8, and 9 of the ASTER sensor were selected. In addition, for enhancing index minerals of phyllic and argillic alterations, bands 4, 5, 6, and 7 of the ASTER sensor were chosen for PCA analysis using the Crosta method.

Table 4- Selected PCA loadings for bands 6, 7, 8, and 9 of ASTER sensor for enhancing propylitic alteration

Eigenvector	Band6	Band7	Band8	Band9
Pc1	0.437702	0.4372599	0.440263	0.650685
Pc2	-0.290505	-0.459658	-0.568818	0.753853
Pc3	0.727972	0.021277	-0.684039	-0.041157
Pc4	-0.440546	0.772701	-0.449702	0.081368

Table 5- Selected PCA loadings for bands 4, 5, 6 and 7 of ASTER sensor for enhancing phyllic and argillic alterations

Eigenvector	Band4	Band5	Band6	Band7
Pc1	0.564241	0.461228	0.486312	0.482081
Pc2	0.817560	-0.424302	-0.307423	-0.432175
Pc3	0.104844	-0.387746	-0.508745	0.761472
Pc4	-0.047278	0.765905	-0.640445	-0.31373

According to Table 4, PC2 has the highest positive loading on band 9 and the highest negative loading on band 8 which aligns with the reflectance and absorption of band 9 and band 8, respectively. Consequently, propylitic alteration is represented with bright pixels (Fig. 7). Considering the data in Table 5, PC3 loading indicates a positive correlation with band 7 and a negative correlation with band 6 which is consistent with the reflectance (band 7) and absorption (band 6) of phyllic alteration. Thus, phyllic alteration is observed with bright pixels in this image. PC2 loadings also align with the absorption and reflectance bands of argillic alteration (bands 4 and 5) and indicate this alteration with bright pixels (Fig. 8).

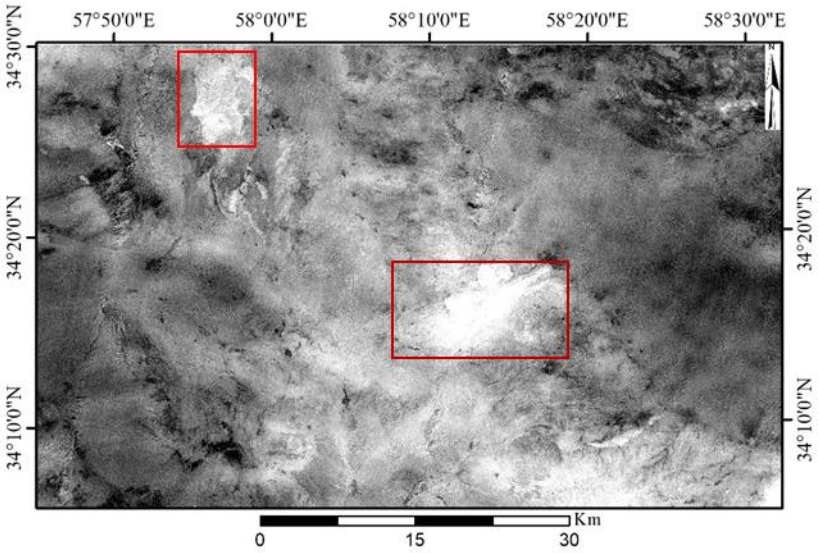

Figure 7- Image corresponding to PC2 of propylitic alteration using Crosta method of ASTER bands 6, 7, 8, and 9. Areas with propylitic alteration are indicated with a red border.

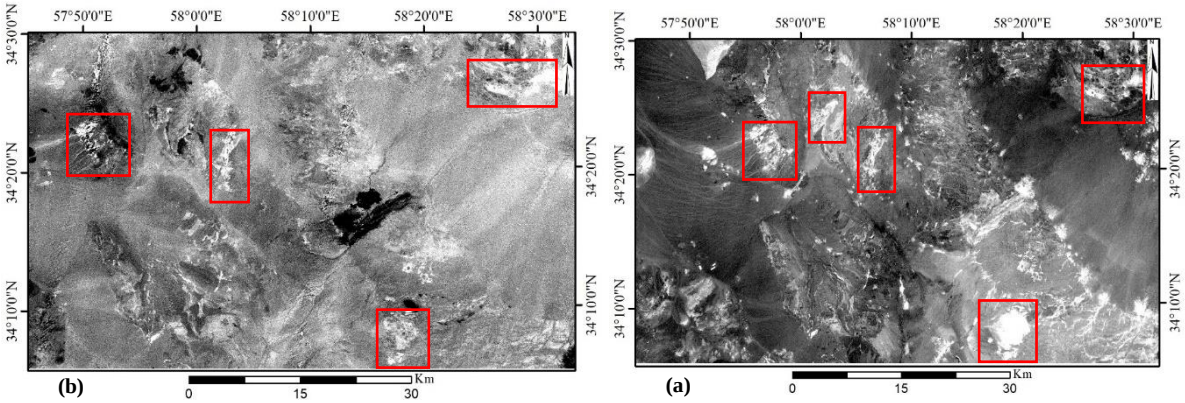

Figure 8- a) PC3 for argillic alteration and b) PC2 for phyllic alteration using the Crosta method of ASTER bands 4, 5, 6, and 7. Target areas are highlighted with a red border in both images.

4.5. Extraction of Lineaments and Calculation of PF

Faults and fractures in the Earth's crust provide suitable pathways for circulating metal-bearing solutions for redistributing various minerals. Therefore, finding the relation between hydrothermal alterations and faults/fractures in an area is of great importance. Sentinel-2A images were used to identify and delineate structural features of the region. For this purpose, directional filters with angles of 45° and 90°, as well as Sobel non-directional filters were used to delineate faults in the region (Figure 9a). Figure 9b presents IDW interpolating of the PF result. Accordingly, areas with the highest density of faults are highlighted with bright pixels.

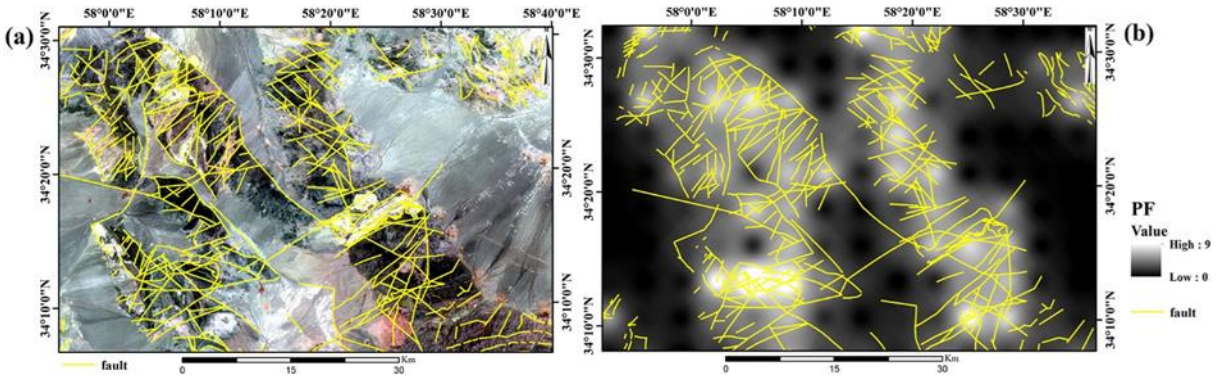

Figure 9- a) Extracted faults from the area overlaid on the ASTER image. b) Interpolated map of the PF analysis.

4.6. Geochemical Anomalies

The differentiation of geochemical anomalies from the background was done for Au, Ag, As, Co, Cu, Fe, Mo, Pb, V, and Zn elements in the stream sediment samples. The results indicate that the highest anomalies are associated with elements Fe, Pb, and Zn while the lowest anomalies are registered for elements Cu, Co and Au.

The element Au exhibits the highest anomalies in dacite, andesite, and rhyolite units. These anomalies are unrelated to the region's alterations. The element Ag shows anomalous occurrences in andesitic and dacitic rock units with argillic and phyllic alterations. The As element displays anomalies in limestone-shale, sandstone, granite, and microgranite units which are associated with intense argillic and phyllic alterations. Additionally, rock samples exhibit an anomaly of As. Co anomaly is observed in carbonate, shale, and limestone units that do not demonstrate alteration. However, in quartz monzonite units, Co indicates anomalies which are associated with phyllic and argillic and to some extent propylitic alterations. The element Cu shows the highest anomalies in andesitic, dacitic, and rhyolitic units which are unrelated to the region's alterations. On the other hand, rock samples indicating the highest Cu content are associated with phyllic and argillic alterations in quartz monzonite units. Anomalies of the element Fe are mostly observed in andesitic and rhyolitic units and are linked to phyllic and argillic alterations. Rock sampling from these areas also indicates Fe anomalies. The element Mo exhibits the highest anomalies in andesitic units where no alteration is observed. Rock sampling from quartz monzonite units indicates Mo anomalies associated with propylitic alterations in the area. Pb anomalies are observed in quartzite and sandstone units while rock samples indicating Pb anomalies are found in sandstone, limestone, and quartz monzonite units. The V element displays anomalies in limestone, shale, sandstone, and granite units, some of which are associated with propylitic and argillic alterations. Rock sampling also shows V anomalies. Zn anomalies are observed in quartz monzonite and conglomerate units and sampling from this area approves Zn anomalies.

4.7. Analytical Hierarchy Process (AHP)

The AHP method can be useful when the decision-making process is faced with several options and decision indicators. Indicators can be quantitative or qualitative. This method is based on paired comparisons (Rozali et al., 2023). To properly valuation of each layer including geology, hydrothermal alteration, structural, and geochemistry layers, a questionnaire was designed and distributed to several experts. The average responses were then inputted into the Expert Choice software and the inconsistency rate was calculated. When the inconsistency rate is 1.0 or less, it shows compatibility in comparing criteria and the validity and value of the findings obtained from the questionnaire the calculated inconsistency rate was 0.2 in this study (Fig. 10).

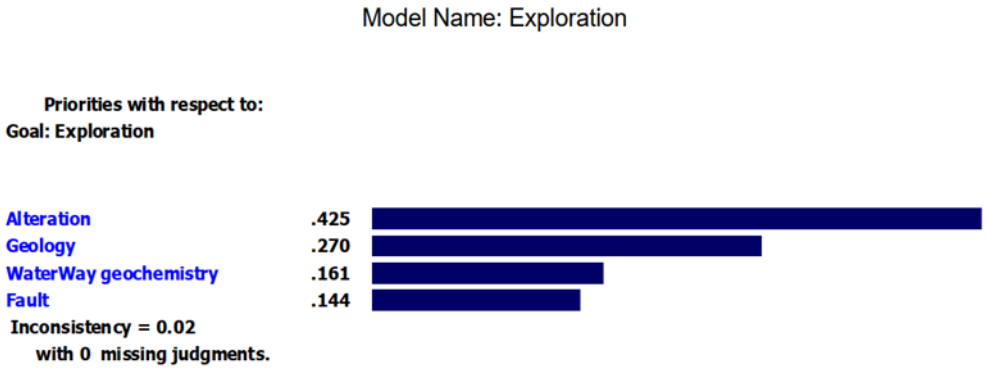

Figure 10- Inconsistency rate calculated for criteria in Expert Choice software

Evidence layers for data integration encompass the region geological map, alteration maps, geochemical maps of stream sediments, and PF. In the geological map, lithological units were categorized into 9 classes, including altered acidic intrusive bodies, unaltered acidic intrusive bodies, extrusive acidic rocks, intermediate rocks, mafic rocks, carbonate rocks, clastic rocks, pyroclastic units, and alluvial deposits. These units are valued on a scale from 0.1 to 0.9 based on their importance in ore mineralization; for example, intrusive acidic bodies with geochemical anomalies are assigned a value of 0.9. The valuation of other units was done similarly. Considering the region's geology and geochemical anomalies, the probability of mineralization is higher in association with phyllic and argillic alterations. In the alteration map, phyllic alteration is valued at 0.9, argillic alteration at 0.8, propylitic alteration at 0.7, and background at 0.1. These weights are based on the significance of each alteration type and their relation to the type of mineralization in the region. The PF map, which is calculated according to density, length, and number of faults in each cell, is categorized into 9 value classes from 0.1 to 0.9. Areas with higher density, length, and number of faults are assigned a value of 0.9 while areas without faults are assigned a value of 0.1, and the remaining areas are classified into different classes based on the density, length, and number of faults. Geochemical interpolation maps were integrated using the fuzzy method and the final map was categorized into 7 classes from 0.1 to 0.7. Finally, the calculated values with the AHP method were multiplied in GIS software across layers and all layers were summed up (Fig. 11).

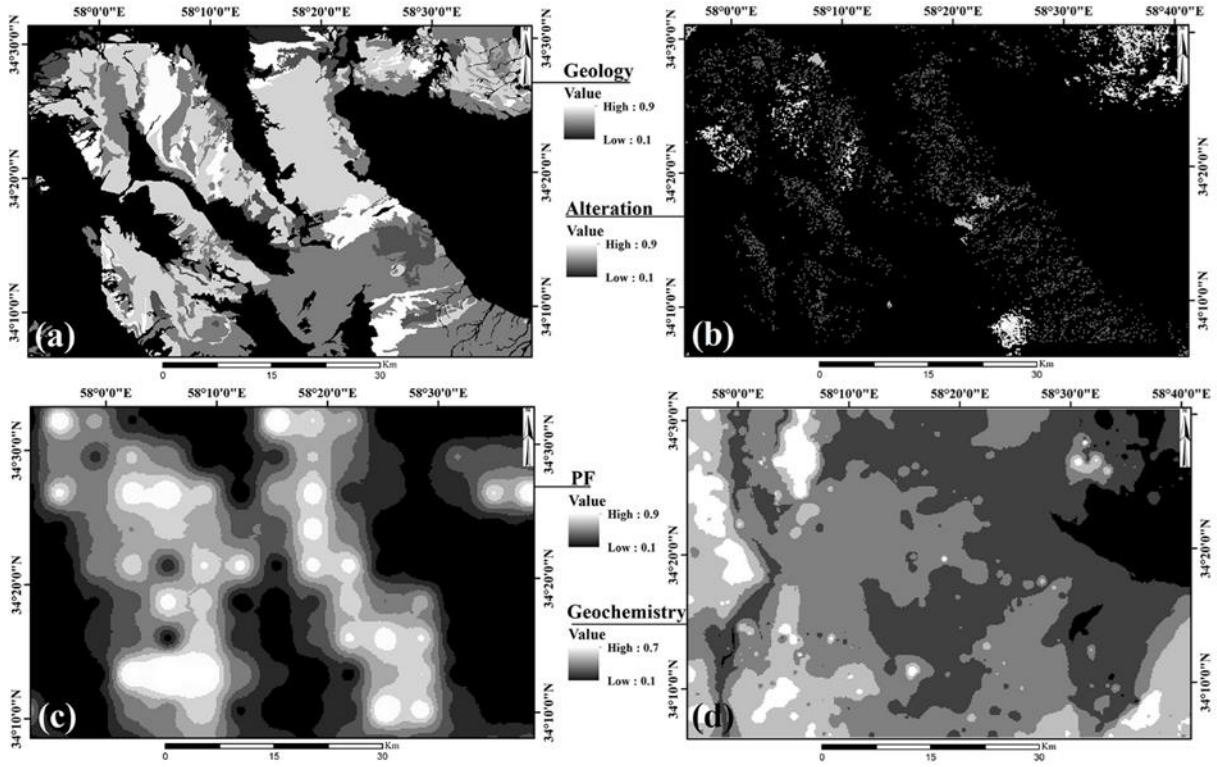

Figure 11- Fuzzy geographical dataset for data integration. a) geological layer, b) alteration layer, c) PF layer and d) geochemical layer

5. Discussion

According to the results derived from the integration of layers and comparison with the geology, the red-colored areas predominantly represent regions with lithological units of rhyolite, granite, and andesite which exhibit phyllic, argillic, and partially propylitic alterations (Figure 12). These areas have a high density of faults. Area A is characterized by rhyolite lithology with iron content ranging from 33706 to 45300 ppm and zinc content of 134-168 ppm. Phyllic, argillic, and partially propylitic alterations are observed in this area. Area B comprises andesite and sandstone lithologies and exhibits phyllic and argillic alterations. Iron slag was observed during field visits in this area. Area C exhibits rhyolite lithology with phyllic and argillic alterations and its iron content ranges from 33706 to 45300 ppm. Area D is characterized by granitic lithology with intense phyllic and argillic alterations. Lastly, Area E consists of andesite, trachyandesite, and basalt with phyllic, argillic, and partially propylitic alterations.

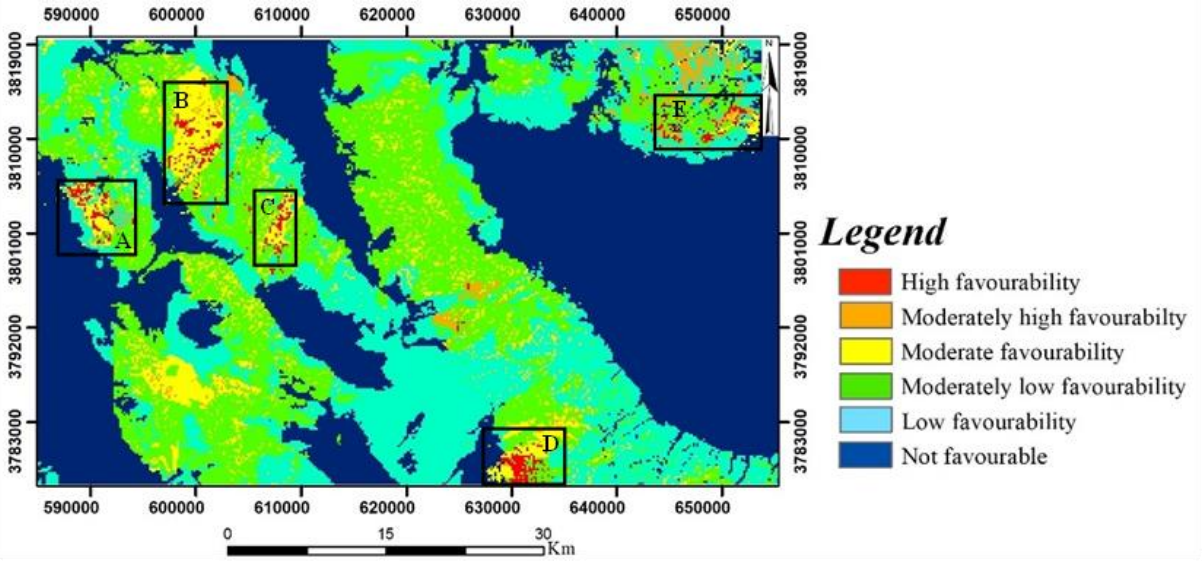

Figure 12- Final image obtained from the summation of weighted layers using the AHP method in the Ferdows-Gonabad-Bajestan region in areas A, B and C

A field investigation was conducted in the area to validate the results. Traces of iron slag, immature gossans, intense alterations, and box-like structures in rocks indicating leaching of metallic elements were observed during the field visit. Figure 13 displays siliceous veins belonging to the 'A' area along with the thin section and the XRD analysis result. The primary lithological units of this area are quartz monzonite, lithic tuff, and their phyllic and argillic alterations. Figure 14 provides an overview of area B and the iron slag along with a thin section prepared from samples of this area and its XRD analysis result. The main lithological units of area B include andesite and sandstone with phyllic and argillic alterations (Fig. 14). Figure 15A corresponds to area C and indicates a general view of the area and its alterations. Figure 15B shows an immature gossan and Figure 15C depicts a location where rock samples have metallic elements such as pyrite. The microscopic image and its XRD analysis result for this area are provided in Figure 15. The main lithological unit of area C is rhyolite with phyllic, argillic, and partially propylitic alterations. Figure 16 pertains to area E with the corresponding thin section image and its XRD analysis result. The main lithological unit of this area is granite accompanied by intense phyllic and argillic alterations. Area F consists of andesite, trachyandesite, and basalt lithologies with phyllic, argillic, and partially propylitic alterations. Currently, a fire clay mine is in operation in this area.

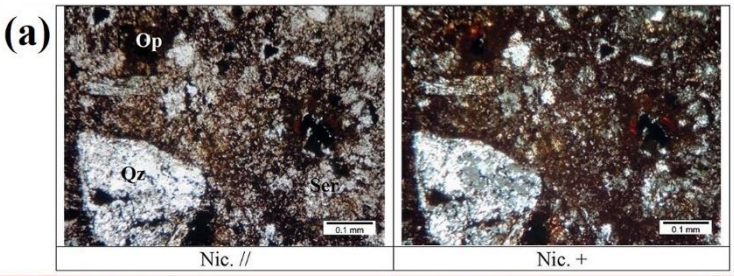

(b)

Sample:	Major Phase(s)	Minor Phase(s)	Trace Phase(s)
G-2	Quartz (33-1161)	Potassium Feldspar	--
LAB: G2-172	SiO2	KAlSi3O8	
Date :	Albite (09-0466)	Muscovite - illite (26-0911)	
19.4.2021	NaAlSi3O8	KAl2Si3AlO10(OH)2	
kV = 40	Calcite (05-0586)	Chlorite (29-0701)	
mA = 30	CaCO3	(Mg,Fe)6(Si,Al)4O10(OH)8	
Ka. = Cu		Goethite (29-0713)	
Fil. = Ni		FeO(OH)	

Figure 13- A) A microscopic image depicts lithic tuff characterized by its main mineral composition of quartz, feldspar, and plagioclase along with secondary minerals such as sericite, apatite, and silica veins. B) XRD analysis related to a rock sample from area A.

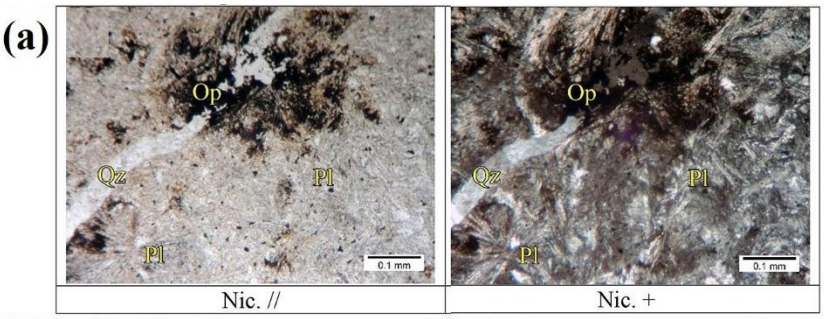

(b)

Sample:	Major Phase(s)	Minor Phase(s)	Trace Phase(s)
F-3	Quartz (33-1161)	Natrojarosite (36-0425)	--
LAB: F3-172	SiO2	NaFe3(SO4)2(OH)6	
Date :	Albite (09-0457)	Kaolinite (29-1488)	
19.4.2021	(Na,Ca)(Si,Al)4O8	Al2Si2O5(OH)4	
kV = 40	Muscovite - illite (26-0911)	Goethite (29-0713)	
mA = 30	KAl2Si3AlO10(OH)2	FeO(OH)	
Ka. = Cu		Potassium Feldspar	
Fil. = Ni		KAlSi3O8	

Figure 14- A) A microscopic image from a basalt sample (spilitic basalt) with main minerals of plagioclase and secondary minerals of apatite, silica evident as veins and fillings within cavities. B) XRD analysis of a rock sample from area B.

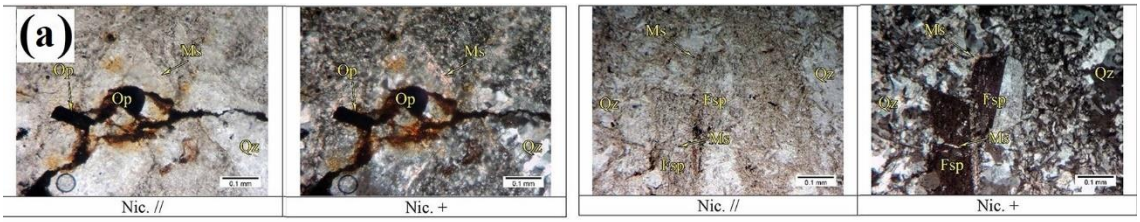

Sample:	Major Phase(s)	Minor Phase(s)	Trace Phase(s)
E-2	Quartz (33-1161)	Muscovite - illite (26-0911)	Hematite (33-0664)
LAB: E-2	SiO2	KAl2Si3AlO10(OH)2	Fe2O3
Date :	Albite (09-0466)	Potassium Feldspar	
19.4.2021	NaAlSi3O8	KAlSi3O8	
kV = 40			
mA = 30			
Ka. = Cu			
Fil. = Ni			

Figure 15- A) A microscopic image from rhyolite having the main mineral composition of quartz, feldspar, and plagioclase along with clay minerals, sericite, apatite, and silica veins as secondary minerals. B) XRD analysis of a rock sample from area C.

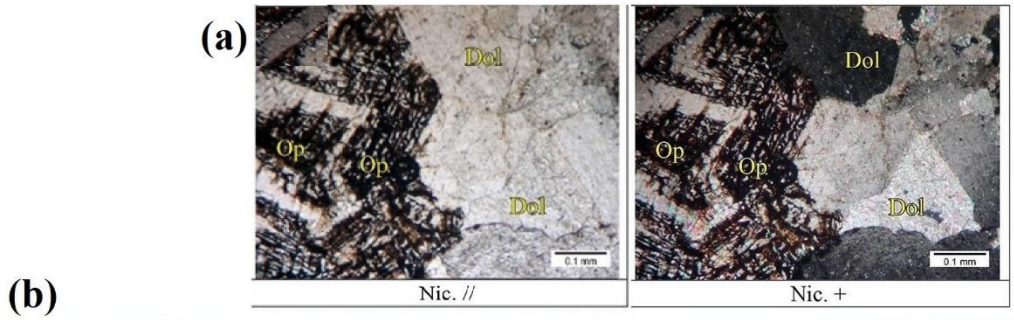

Sample:	Major Phase(s)	Major Phase(s)	Minor Phase(s)
A-Z	Quartz (33-1161)	Dolomite (36-0426)	Goethite (29-0713)
LAB: AZ-172	SiO2	CaMg(CO3)2	FeO(OH)
Date :	Calcite (05-0586)	Chlorite (29-0701)	
19.4.2021	CaCO3	(Mg,Fe)6(Si,Al)4O10(OH)8	
kV = 40	Albite (09-0466)		
mA = 30	NaAlSi3O8		
Ka. = Cu	Muscovite - illite (26-0911)		
Fil. = Ni	KAl2Si3AlO10(OH)2		

Figure 16- A) A microscopic image related to a dolostone with main minerals of dolomite, quartz, calcite, and secondary minerals of apatite and calcite. B) XRD analysis of a rock sample from area E.

Table 6 examines the accuracy of the final alteration map results. For this purpose, sample points collected from the area have been utilized.

Table 6- Examination of processing errors

	Phyllic alteration	Argillic alteration	Propylitic alteration	Oxid iron	Unaltered	Total	User Acc (%)
Phyllic alteration	8	0	0	2	0	10	80.00
Argillic alteration	0	8	0	0	0	8	90.00
Propylitic alteration	0	0	6	0	0	6	90.00
Oxid iron	0	0	0	6	0	6	80.00
Unaltered	0	0	0	0	10	15	99.00
Total	9	11	7	9	15	51	
Prod. Acc (%)	8/9	8/11	6/7	8/9	10/15		

Overall accuracy = (48/51) 90.04% **Kapa coefficient = 0.89**

Based on the information provided in Table 5, the accuracy of the findings in the final map is 90% with a kappa coefficient of 0.89. These values indicate the accuracy of the results.

6. Conclusion

Based on the results derived from stream sediment and lithological units, high concentrations of lead, zinc, and iron are observed in areas with limestone, rhyolite, and tuff as 20317-73330 ppm, 38820-191000 ppm and 45300-33706 ppm respectively. This suggests the possibility of polymetallic mineralization in the region. Moreover, the alignment of these anomalies with the results of satellite image processing in the area strengthens the possibility of the existence of lead and zinc veins in hydrothermal sedimentary and igneous rocks. The presence of iron slag, gossan, and intense alterations further support this hypothesis. The integration of alteration layers, geochemical data, the PF of the area, and geological maps using the AHP method resulted in the identification of five potential areas for mineralization. Microscopic examination and XRD analysis of the samples were conducted to validate the results. Areas A, B, and C, due to their higher elemental concentrations, high fault density, and intense phyllic and argillic alterations are classified as the priority for mineralization. The use of shortwave infrared images from the ASTER sensor for identifying alterations, OLI images for identifying iron oxides, and Sentinel-2A, SPOT5, and IRS images for identifying geological units, faults, and streams in areas with similar geology is recommended.

7. Acknowledgment

Sincere thanks and appreciation are extended to Golgohar Sirjan Mining and Industrial Company for their financial and moral support.

8. References

1. Abrams M, Tsu H, Hulley G, et al, The advanced spaceborne thermal emission and reflection radiometer (ASTER) after fifteen years, review of global products, Int J Appl Earth Obs Geoinf 2015, 38, 292–301.

2. Ahmadirouhani,R. Karimpour,M.H. Rahimi,B. Malekzadeh-Shafaroudi,A. Beiranvand Pour,A. Pradhan,B (2018): Integration of SPOT-5 and ASTER satellite data for structural tracing and hydrothermal alteration mineral mapping: implications for Cu–Au prospecting, International Journal of Image and Data Fusion, DOI:10.1080/19479832.2018.1469548.

3. Aghanabati.A, 2006. Geology of Iran. Ministry or industry & mine geological survey of Iran.

4. Arjmand Lary, Z. Honarmand, M. Shahriari, H. Hosseinjani Zadeh, M. 2023. Data integration by fuzzy logic for mineral prospectivity mapping in Ferdows-Gonabad-Bajestan belt, Khorasan Razavi Province, Iran. Journal of Geological Remote Sensing, ID: JGRS-2310-1006.

5. Carrino.T.A, Crosta.A.P, Toledo.C.L.B, Silva.A.M, Silva.J.L;2015. Geology and hydrothermal alteration of the Chapi Charia perospect and nearby target, southern peru, using ASTER data and reflectance spectroscopy.

6. Drury.S.A., Image Interpretation in Geology, Chapman and Hall,London, 1993, p.283.

7. Fujisada H, Design and performance of ASTER instrument, In, Advanced and next-generation satellites. International Society for Optics and Photonics, 1995, 16–26.

8. Ghorbani, A., Honarmand, M., Shahriari, H., & Hassani, M. J. (2019). Regional scale prospecting for non-sulphide zinc deposits using ASTER data and different spectral processing methods. International journal of remote sensing, 40(23), 8647-8667.

9. Ghodsi Pore., S. H., (1381). Hierarchical analysis process. Tehran. Amir Kabir University Press.

10. Gupta, R.P., 2003 Remote Sensing Geology, Second edition, Springer, Verlag, Berline, 656 p.

10. Honarmand,M . Ranjbar,H. Shahabpour,J., 2011. “Application of Spectral Analysis in Mapping Hydrothermal Alteration of the Northwestern Part of the Kerman Cenozoic Magmatic Arc, Iran”. Journal of Sciences, Islamic Republic of Iran 22(3): 221-238.

11. Honarmand M, Ranjbar H, and Shahabpour J; 2012. Application of Principal Component Analysis and Spectral Angle Mapper in the Mapping of Hydrothermal Alteration in the Jebal– Barez Area, Southeastern Iran.

12. Honarmand, M., Ranjbar, H. and Shahabpour, J., 2013. " Combined use of ASTER and ALI data for hydrothermal alteration mapping in the northwestern part of the Kerman magmatic arc, Iran", International Journal of Remote Sensing, 34, 2023- 2046.

13. Hardcastle, K. C., Emery, J. M., Tinkham, D. J. & Brooks, J. A., 1997- Photolineament Factor Analysis: A new computerized method of remotely assessing the degree to which bedrock is fractured, NWWA Conf. Innov. Ground Water Tech. of the 90’s.

14. Hardcastle, K., et al., "Photolineament Factor Analysis: A new computerized method of remotely assessing the degree to which bedrock is fractured, NWWA Conf. Innov". Ground Water Tech. of the 90's, 1997.

15. Mars, John C., Rowan, Lawrence C., 2006, "Regional Mapping of Phyllic- and Argillic-Altered Rocks in the Zagros Magmatic arc, Iran, using Advanced Spaceborne Thermal Emission and Reflection Radiometer (ASTER) Data and Logical Operator Algorithms", Geosphere 2, PP. 61-186.

16. Mousavi, S. S., Honarmand, M., Shahriari, H., & Hosseinjanizadeh, M. (2019). Mineral exploration modeling of metallic deposits using ASTER and OLI images for producing mineral potential map in Esfandaghe region, Kerman province. Scientific Quarterly Journal of Geosciences, 29(113), 45-56.

17. Ranjbar, H., & Shahriari, H. (2006). Comparison of ETM+ and ASTER data for hydrothermal alteration mapping in the central part of the Dehaj-Sarduyeh belt, Kerman Province. Iran. J. Crystallogr. Mineral, 14(2), 367-382.

18. Roy DP, Wulder MA, Loveland TR, et al, Landsat-8, Science and product vision for terrestrial global change research, Remote Sens Environ 2014, 145, 154–172

19. Rozali, C. Zein, A. Farizy, S. "PENERAPAN ANALYTIC HIERARCHY PROCESS (AHP) UNTUK PEMILIHAN PENERIMAAN KARYAWAN BARU". 2023. JITU: Jurnal Informatika Utama Hal. 32-36. DOI: https://doi.org/10.55903/jitu.v1i2.153. 27

20. Shahriari, H., Honarmand, M., & Ranjbar, H. (2015). Comparison of multi-temporal ASTER images for hydrothermal alteration mapping using a fractal-aided SAM method. International Journal of Remote Sensing, 36(5), 1271-1289.

21. Tangestani, M. H., Moore, F., 1002, Porphyry copper potential mapping using the weights-of-evidence model in a GIS, northern Shahr-e-Babak, Iran, Porphyry copper potential mapping using the weights-of- evidence model in a GIS, northern Shahr-e-Babak, Iran, Volume 84, Issue 5. 40:121-771.

22. Tözün, K.A. Özyavaş, A. New logical operator algorithms for mapping of hydrothermally altered rocks using ASTER data: a case study from central Turkey, Ore Geology Reviews (2020), doi: https://doi.org/10.1016/j.oregeorev.2020.103533.